Article

Synthesis and Characterization of Thermoelectric Co$_2$XSn (X = Zr, Hf) Heusler Alloys

Alessandro Difalco [1] [iD]**, Francesco Aversano** [1]**, Stefano Boldrini** [2]**, Alberto Ferrario** [2] [iD]**,
Marcello Baricco** [1] [iD] **and Alberto Castellero** [1,*]

[1] Dipartimento di Chimica and NIS, Università di Torino, Via P. Giuria 7, 10125 Torino, Italy;
alessandro.difalco@edu.unito.it (A.D.); francesco.aversano@unito.it (F.A.); marcello.baricco@unito.it (M.B.)

[2] CNR–ICMATE, Padova Unit, Corso Stati Uniti 4, 35127 Padova, Italy; stefano.boldrini@cnr.it (S.B.);
alberto.ferrario@cnr.it (A.F.)

[*] Correspondence: alberto.castellero@unito.it; Tel.: +39-011-6707097

Abstract: In this work, we report the results of an experimental investigation on the synthesis, structure, microstructure, mechanical, electrical conductivity, and Seebeck coefficient of Co$_2$XSn (X = Zr, Hf) alloys. In both the alloys, the main constituent is a full Heusler-type compound that coexists with small amounts of secondary phases. Both alloys show a rather high Vickers hardness (around 900 HV) and an indentation fracture toughness typical of ceramics (around 2 MPa·m$^{1/2}$). The electronic transport properties of the two alloys were measured for the first time. The temperature dependence of both the Seebeck coefficient and the electrical conductivity of the two alloys shows a change in correspondence of the Curie temperature. The Seebeck coefficient reaches a constant plateau, while the electrical conductivities show a transition from metallic to semiconductor behavior. As a consequence, almost constant values of the power factor have been obtained for the power factor above the Curie temperature, which is promising for an efficient exploitation of thermal gradients of several hundreds of degree in waste heat harvesting applications. Finally, on the basis of results from this work and from the literature, the effect of the substitution of the X element on the electronic transport properties in the series Co$_2$XSn (X = Ti, Zr, Hf) is discussed.

Keywords: Heusler; arc melting; Seebeck; electrical conductivity; thermoelectric; Curie temperature

1. Introduction

The Heusler alloys represent an important class of thermoelectric materials since they generally combine good performances with high thermal stability, and, in most cases, ease of synthesis. The structure of the full-Heusler (FH) compounds consists of 4 FCC sublattices with a L2$_1$-type structure, while the one of the half-Heusler (HH) compounds consists of 3 FCC sublattices arranged according to the C1b lattice prototype [1]. On the one hand, HH alloys show remarkable zT values such as 1.5 for (Zr$_{0.5}$Hf$_{0.5}$)$_{0.5}$Ti$_{0.5}$NiSn$_{0.998}$Sb$_{0.002}$ [2] and Nb$_{0.88}$Hf$_{0.12}$FeSb [3], and about 1.2 for Ti$_{0.5}$Zr$_{0.5}$NiSn$_{0.98}$Sb$_{0.02}$ [4] and densification-aided Ti$_{0.5}$Zr$_{0.5}$NiSn [5]. On the other hand, FH alloys exhibit numerous worthwhile properties related to their particular electronic structures. For example, Co-based FH alloys are proved to be half-metallic ferromagnets, and they display an electronic density of states (DOS), which leads to the manifestation of spin-Seebeck effects [6–8]. For this reason, the Co-based full-Heusler compounds can be promising materials for application in spintronics and spin-caloritronics [7,9–11].

One of the first investigation on Co-based FH alloys was the work of Ziebeck and Webster [12] in 1974, where both the structural characterization by means of neutron diffraction and the magnetic properties are reported. Later, in 1987, De Souza et al. [13] confirmed the magnetic properties reported

in Ref. [12]. Furthermore, they reported a Curie temperature (T_C) of 460 K for Co_2ZrSn and 423 K for Co_2HfSn.

As far as the thermoelectric properties are concerned, Barth et al. [14] investigated the magnetic and electronic transport properties of the Co_2TiZ (Z = Si, Ge, Sn) alloys and reported a maximum value of thermopower of about −50 μV/K (which is quite high for a metallic compound) together with a T_C of 360 K for the Co_2TiSn alloy. Moreover, they highlighted that a remarkable characteristic of these materials is the fact that the absolute value of the Seebeck coefficient linearly increases up to T_C, and then it settles in a plateau and remains constant throughout the entire analyzed range of temperature. They suggested also that this anomalous trend of the Seebeck coefficient can be explained by the half-metallic behavior of the Co-based family of FH alloys. Concerning the electrical conductivity (σ), Co_2TiSn exhibits a relatively small value of 2851 S/cm after T_C, which is the smallest of all compounds investigated in that work.

It is also important to mention that the band structures and the electronic DOS of the Co_2XSn (where X is a metal of group 4 of the periodic table, namely Ti, Zr, and Hf) alloys have been studied in several theoretical investigations [6–9,15–17]. There is a general agreement on the fact that all the three alloys show an electronic DOS typical of half-metallic ferromagnets. This particular property manifests itself in magnetic compounds with an electronic DOS consisting in quite continuous majority-spin sub-bands and minority-spin sub-bands that instead exhibit semiconductor-like band gaps [6]. This property would allow these compounds, at least below T_C, to generate spin-Seebeck effects [6–9], which can be described as the ability of a material to conduct spin-polarized electrons when the system is subjected to thermal gradients [7,10]. Despite these promising properties, until now, there have been no significant advances in the determination of the transport properties of the Co_2XSn compounds.

On the one hand, mechanical properties are useful for evaluating the reliability of materials when assembled in a thermoelectric module. On the other hand, since the understanding of the thermoelectric properties of the Co-based FH alloys is still lacking, it is valuable to gather as much information as possible on the behavior of these compounds in view of spintronic and waste heat harvesting applications. Thus, the aim of this work is to measure for the first time the mechanical properties (i.e., Vickers hardness, indentation fracture toughness) and electronic transport properties (i.e., Seebeck coefficient, electrical conductivity) of the Co_2ZrSn and Co_2HfSn alloys. Furthermore, considering the properties of the Co_2XSn (X = Ti, Zr, Hf) series of FH alloys, it is discussed how the electronic transport properties may vary when the X metal is changed.

2. Materials and Methods

The pure elements were weighted in the appropriate stoichiometric quantities and melted in the arc furnace (Edmund Bühler GmbH, Bodelshausen, Germany). Due to the large difference in the melting points of Zr/Hf and Sn, two pre-alloys were synthesized for each FH system, namely CoZr and CoSn for Co_2ZrSn, and CoHf and CoSn for Co_2HfSn, to guarantee a better homogenization of the melt. Pre-alloys were melted together several times in order to obtain homogeneous samples. Then, the ingots were wrapped in tantalum foils, sealed in evacuated quartz tubes, and annealed at 800 °C for 6 days.

X-ray diffraction (XRD) investigation was performed in Bragg–Brentano configuration with a X'Pert Pro diffractometer (PANalytical B.V., Almelo, The Netherlands) using a Cu-Kα radiation as the X-ray source. For the XRD analysis, the samples were crushed in thin powders to remove the effect of possible preferred crystallographic orientations. The Rietveld refinements of the XRD patterns were performed with the MAUD software [18]. The surface analysis was executed by Scanning Electronic Microscopy (SEM) with an EVO 50 microscope (Carl Zeiss Microscopy GmbH, Jena, Germany) equipped with an Inca Energy 250 Energy Dispersion Spectrometer (EDS) under vacuum of 10^{-6} mbar, 20 kV of potential, and 150 pA of current. All the SEM images presented in this work were collected

in backscattered electrons (BSE) mode on mechanically polished surfaces. The XRD and SEM-EDS investigations were performed on both the as-cast and annealed specimens.

Microhardness measurements were performed on the annealed samples with a microhardness tester (Buehler, Lake Bluff, IL, USA) using a load of 4.9 N. The length of the indent diagonals and crack length were measured using a DMLM optical microscope (Leica, Wetzlar, Germany). The error associated with the mechanical properties was calculated using the standard t-student type formula for independent measurements, or $Er = SDt/n^{1/2}$ (where Er is the obtained error, SD is the standard deviation, t is the tabulated t-student value relative to a confidence interval of 95%, and n is the number of independent measurements). The densities of the two alloys were measured by weighting ingots of known volume and by the Archimedes principle using a pycnometer.

The Seebeck coefficient and electrical conductivity were measured on bar-shaped annealed samples ($12 \times 2 \times 2$ mm^3) under He flow between room temperature and 778 K by using a custom test apparatus described in ref. [19]. Furthermore, in order to assess the thermal stability of the alloys, the properties were measured upon heating and cooling.

3. Results and Discussion

3.1. Structural and Microstructural Characterization

The XRD patterns of both annealed alloys are shown in Figure 1. The XRD patterns of the as-cast alloys are shown in the supplementary materials (Figure S1). Figure 2a,b and Figure 2c,d show the backscattered SEM images of annealed Co$_2$ZrSn and Co$_2$HfSn ingots, respectively, where the gray contrast suggests the homogeneous distribution of two secondary phases immersed in the main phase. The same SEM images relative to the as-cast alloys can be found in the supplementary materials (Figures S2 and S3). Table 1 shows the results of the Rietveld refinement of the XRD patterns shown in Figure 1 and the EDS elemental compositions of the phases observed in Figure 2, which are all related to the annealed samples, together with the results of the same investigations performed on the as-cast alloys. As reported in Table 1, both the Rietveld refinement and the EDS investigation indicate that phase 1 and 4 correspond to the Co$_2$ZrSn and Co$_2$HfSn full Heusler structures, respectively, and they represent the main component of each alloy. In the case of Co$_2$ZrSn alloy, phases 2 and 3 are found to be the binary compounds Co$_2$Zr and CoSn, respectively. In the case of Co$_2$HfSn alloy, phases 3 and 5 are the binary compounds CoSn and Co$_2$Hf, respectively. In addition, Ziebeck and Webster [12] reported the presence of secondary phases, together with the FH phase even after annealing.
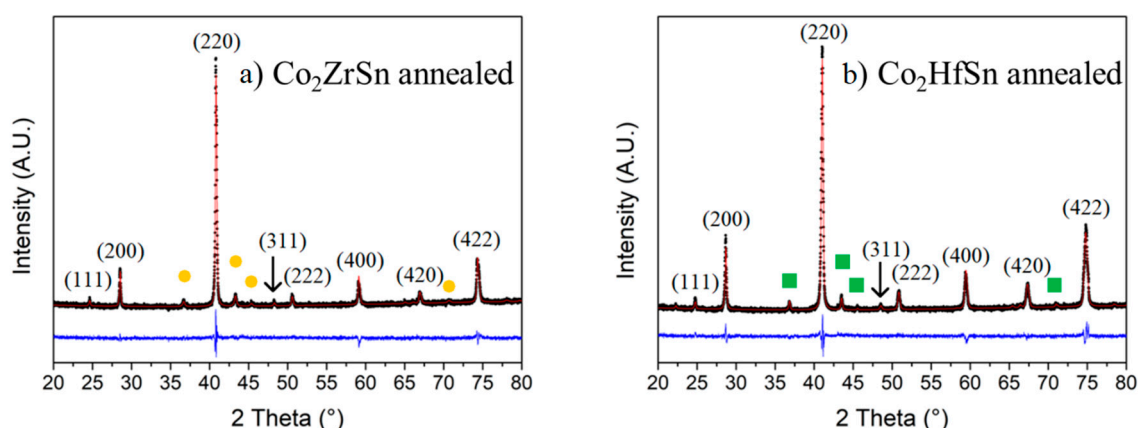

Figure 1. XRD patterns and Rietveld refinements of the Co$_2$ZrSn (**a**) and Co$_2$HfSn (**b**) annealed alloys. The black symbols and the red continuous line are the experimental and the calculated patterns respectively, while the blue line represents the difference between the two. The peaks proper of the full-Heusler phases are marked with their relative Miller indexes, whereas the signals of the secondary phases are highlighted with colored shapes (orange circles for Co$_2$Zr and green squares for Co$_2$Hf).
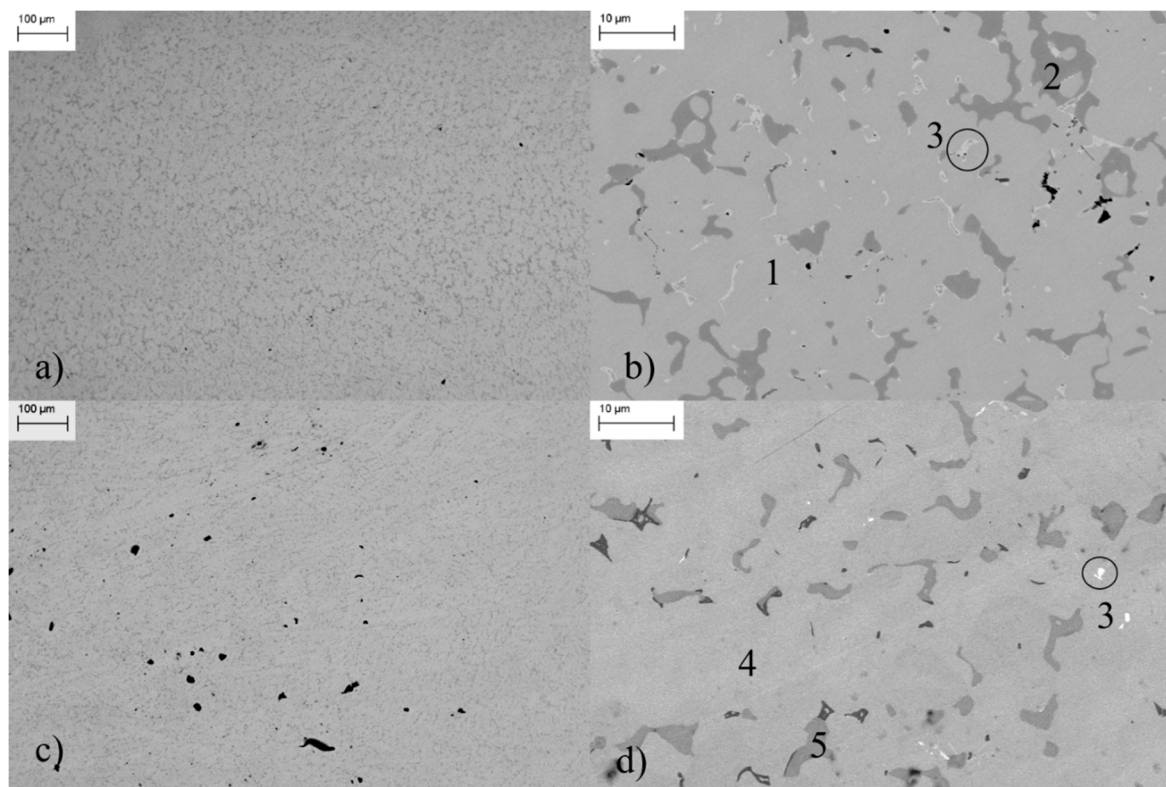
Figure 2. Backscattered electrons SEM images of the Co$_2$ZrSn (**a**,**b**) and Co$_2$HfSn (**c**,**d**) annealed alloys. In accordance with the results of the Rietveld refinement of the XRD patterns (Figure 1 and Table 1), the observed phases are the L2$_1$-type Co$_2$ZrSn full-Heusler (1), the C15-type Co$_2$Zr (2), CoSn (3), the L2$_1$-type Co$_2$HfSn full-Heusler (4), and the C15-type Co$_2$Hf (5).

Average EDS measurements at low magnifications indicated that the overall composition of the specimens slightly deviates from the nominal stoichiometry. The average atomic compositions of the samples resulted to be 53% Co, 25% Zr, and 22% Sn for the Co$_2$ZrSn sample, and 51% Co, 25% Hf, and 24% Sn for the Co$_2$HfSn alloy, indicating slight Sn depletion and Co excess, with consequent formation of the observed secondary phases.

As reported in Table 1, the Rietveld analysis allowed quantifying the amount of secondary phases in the samples, which is 12% for Co$_2$Zr (2) and 7% for Co$_2$Hf (5). Concerning phase 3 (CoSn), its abundance is too small to be calculated with the Rietveld refinement (so its quantity will be considered negligible). The relative amount of the secondary phases does not change after annealing; however, slight changes of the EDS phase composition and lattice parameters can be observed. The lattice parameters found for the as-cast alloys are 6.2338 Å and 6.2101 Å for Co$_2$ZrSn and Co$_2$HfSn, respectively. After annealing, the values of the lattice parameters become 6.2458 Å for Co$_2$ZrSn and 6.2157 Å for Co$_2$HfSn, which are very close to the equilibrium values reported by Ziebeck et al. [12] (i.e., 6.249 Å and 6.218 Å for Co$_2$ZrSn and Co$_2$HfSn, respectively).

Densities of 9.2 g/cm^3 and 11.7 g/cm^3 were obtained for Co$_2$ZrSn and Co$_2$HfSn samples, respectively. As a result of the presence of secondary phases and the deviation of the phase composition from the stoichiometry (see Table 1), the measured values cannot be compared with the values of crystallographic density for the pristine compounds [20] (i.e., 8.92 g/cm^3 and 11.47 g/cm^3 for Co$_2$ZrSn and Co$_2$HfSn, respectively), and experimental values [12] of monophasic Co$_2$ZrSn (8.90 g/cm^3) and Co$_2$HfSn (11.40 g/cm^3) [12]. Thus, the crystallographic density of each phase was calculated on the basis of the actual composition and the refined lattice parameter. Subsequently, the theoretical densities of the two-phases samples were obtained as the weighted average of the crystallographic density of the phases present in each sample, leading to values of 9.2 g/cm^3 and 11.9 g/cm^3 for the Co$_2$ZrSn and

Co_2HfSn samples, respectively. It follows that the relative densities of Co_2ZrSn and Co_2HfSn samples are 100% and 98%, respectively.

Table 1. Composition, prototype–structure, cell parameters, and relative abundances of the different phases in the Co_2ZrSn and Co_2HfSn samples. The structure of the phase 3, CoSn, is shown as reported in the Co-Sn phase diagrams [21].

Co_2ZrSn As-Cast							
Elemental composition (at %)			Label	Phase	Structure	a (Å)	Abundance (wt %)
Co	Zr	Sn					
45	28	27	1	Co_2ZrSn	$L2_1$	6.2338	88%
65	21	13	2	$Co_2Zr_xSn_y$	C15	6.9174	12%
58	-	42	3	CoSn	B35	-	-
Co_2ZrSn Annealed							
Elemental composition (at %)			Label	Phase	Structure	a (Å)	Abundance (wt %)
Co	Zr	Sn					
46	27	27	1	Co_2ZrSn	$L2_1$	6.2458	88%
66	19	15	2	$Co_2Zr_xSn_y$	C15	6.9212	12%
58	-	42	3	CoSn	B35	-	-
Co_2HfSn As-Cast							
Elemental composition (at %)			Label	Phase	Structure	a (Å)	Abundance (wt %)
Co	Hf	Sn					
45	27	28	4	Co_2HfSn	$L2_1$	6.2101	93%
65	26	9	5	$Co_2Hf_xSn_y$	C15	6.9024	7%
56	-	44	3	CoSn	B35	-	-
Co_2HfSn Annealed							
Elemental composition (at %)			Label	Phase	Structure	a (Å)	Abundance (wt %)
Co	Hf	Sn					
47	26	27	4	Co_2HfSn	$L2_1$	6.2157	93%
66	25	9	5	$Co_2Hf_xSn_y$	C15	6.8915	7%
55	-	44	3	CoSn	B35	-	-

Ultimately, the unaltered relative abundance of the phases before and after the annealing treatment, and the small changes in their elementary composition and in the lattice parameters suggest that the full-Heusler phases 1 and 4 crystallize congruently from the melt with small impurities of secondary compounds Co_2Zr and Co_2Hf (2 and 5 respectively) and small traces of CoSn (3), which is due to the slight deviation of the prepared samples from the nominal stoichiometry. Thus, these alloys can be easily processed by direct solidification of the melt.

3.2. Mechanical Properties

As reviewed by Ponton et al. [22], when the surface of a material is indented, the cracks that propagate from the imprint can be of two different classes: halfpenny type and Palmqvist type. It is known that the halfpenny cracks propagate both on the surface (radial direction) and deeply below (median direction) the imprint. For this reason, they are also called radial-median cracks. Conversely, the Palmqvist type is shallower and includes cracks that do not propagate directly below the indentation, but only in the radial direction. It is possible to distinguish between the two typologies of cracks by performing a light polishing of the surface of the sample after indentation. After the procedure, if the cracks remain visible and always connected to the inverted pyramid of the indent, the behavior can be classified as halfpenny; whereas, a small detachment should be visible in case of cracks of the Palmqvist type, or, alternatively, only the indenter imprint should be observed in case of

very shallow cracks [23–25]. It was also generally observed that fairly shallow Palmqvist-type cracks are expected for hard metallic materials [23].

As expected, significant cracks have been observed after the first indentation, which has been used to determine the hardness, as reported in Table 2. After light polishing of the surface using a 3 μm diamond paste, the radial cracks were no longer visible, indicating that these are extremely shallow. In Figure 3, as an example, one of the several indentations performed for each alloy is shown before and after the polishing treatment. No secondary cracks propagated from the Vickers imprint, which indicates that the whole load was transferred to the radial cracks, allowing an accurate estimation of the fracture toughness (K_{IC}). The same result was observed for all the other indentations.
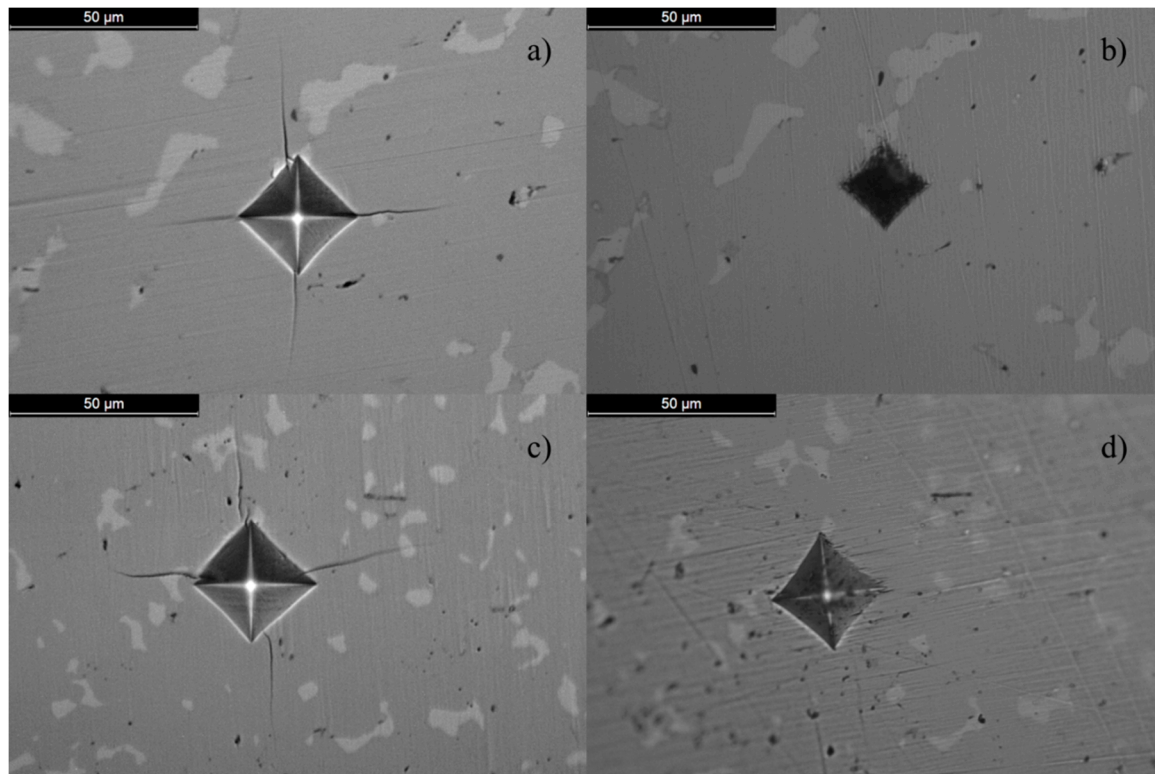

Figure 3. Examples of Vickers indentations on the Co_2ZrSn (panel **a** and **b**) and Co_2HfSn (panel **c** and **d**) alloys before (**a**,**c**) and after (**b**,**d**) light polishing.

Several polishing cycles were performed until the Vickers imprints disappeared (not shown), and also in these cases, no median cracks were observed.

It is possible to distinguish between the two types of cracks from the ratios c/a or l/a (where c is the length of the cracks from the center of the indent to their tip, a is half of the indentation diagonal, and l is the length of the crack measured from the corner of the indent). Being $c = a + l$, it turns out that c/a and l/a are linked by the following relationship $l/a = (c/a) - 1$. According to Refs. [23] and [26], when $c/a \leq 2.5$ (or $l/a \leq 1.5$), the crack should be classified as Palmqvist. Other studies [27,28] fix the upper limit of Palmqvist cracks for values of l/a around 2.5 (or $c/a \leq 3.5$). The l/a ratio was calculated for both the alloys and the values obtained are lower than 1.5 in all the cases (see Table 2).

Therefore, in agreement to the micrographic observations, the cracks can be described as Palmqvist-type, so the fracture toughness K_{IC} can be evaluated using the Shetty–Wright–Mincer–Clauer equation [22,29], which in the case of a standard Vickers indenter is

$$K_{IC} = 0.0319 \cdot \frac{P}{a \cdot l^{1/2}} \tag{1}$$

where P is the applied load.

As reported in Table 2, the two alloys exhibit similar mechanical properties, showing a rather high hardness for metallic compounds and a fracture toughness comparable to those of ceramics [30]. These values are close to those generally exhibited by half Heusler alloys [31], so they can be considered suitable for application in devices.

Table 2. Average values of *l/a* ratios, Vickers hardness, and fracture toughness K_{IC} for the Co_2ZrSn and Co_2HfSn alloys.

Alloy	Hardness (HV)	*l/a*	K_{IC} (MPa·m$^{1/2}$)
Co_2ZrSn	903 ± 31	1.42	2.07 ± 0.23
Co_2HfSn	899 ± 26	1.41	2.06 ± 0.14

3.3. Temperature Dependence of Electrical Conductivity, Seebeck Coefficient, and Power Factor

The trends of the electrical conductivity (σ), Seebeck coefficient (S), and power factor (PF) of annealed Co_2ZrSn and Co_2HfSn ingots as a function of the temperature are shown in Figure 4. The transport properties were measured imposing a cyclic ramp of temperature in order to ensure the thermal stability of the samples and the reproducibility of the results under thermal cycling. Since no hysteresis is observable between heating and cooling, it is confirmed that the specimens are stable and the outputs are reproducible. Values previously obtained for Co_2TiSn [14] are reported for comparison. It should be noted that the values measured in this work refer to samples containing metallic secondary phases (i.e., Co_2Zr and Co_2Hf) [32], which likely tend to increase the electrical conductivity and lower the absolute value of the Seebeck coefficient with respect to the corresponding single-phase materials.

Figure 4a shows that the electrical conductivities of Co_2ZrSn and Co_2HfSn are quite similar to each other. At room temperature (298 K), electrical conductivities values of 4196 S/cm and 4476 S/cm are measured for Co_2ZrSn and Co_2HfSn, respectively. Since for this class of compounds, the Curie point can be determined measuring the point at which σ changes its slope [14], T_C values of 465 K and 426 K have been obtained for Co_2ZrSn and Co_2HfSn, respectively. The electrical conductivity decreases almost linearly as a function of the temperature until T_C is reached, where it exhibits the lowest value, namely 2982 S/cm for Co_2ZrSn and 3046 S/cm for Co_2HfSn. After T_C, the electrical conductivities show a slight increase with the temperature, until values of 3235 S/cm and 3267 S/cm are observed for Co_2ZrSn and Co_2HfSn, respectively, at 778 K. Considering these trends, it is possible to observe that the materials show metallic-like behavior at temperatures lower than T_C, whereas the electrical conductivities switch to a semiconductor-like behavior at higher temperatures. This is a consequence of the ferromagnetic–paramagnetic transition, which strongly influences the electronic DOS of the alloys. These results are in good agreement with those reported by De Souza et al. [13]

The Seebeck coefficient of both alloys is shown in Figure 4b as a function of temperature. It is negative as in the case of Co_2TiSn [14], indicating that the major charge carriers are electrons (n-type). At 298 K, the values of S are -9 $\mu V/K$ and -13 $\mu V/K$ for Co_2ZrSn and Co_2HfSn alloys, respectively. The absolute values of S of two alloys show a linear increase from room temperature to T_C. At higher temperatures, the values of S settle on a plateau at approximately -34 $\mu V/K$ and -38 $\mu V/K$ for Co_2ZrSn and Co_2HfSn samples, respectively. As reported for Co_2TiSn and other types of compounds [14,33,34], a linear increase of Seebeck coefficient followed by a constant value above the Curie temperature can be related to a steady position of the Fermi level over an extended range of temperature.

The behavior of the power factor (PF = $S^2\sigma$) as a function of temperature is similar for the two alloys, as shown in Figure 4c. Between room temperature and T_C, the PF of the two alloys increases as a function of temperature. Above T_C, the PF values for both alloys reach a plateau, which is maintained up to 778 K. The observed behavior strongly reflects the trend of the Seebeck coefficient, which actually gives the main contributions to PF. At room temperature, values of 0.026 mW·m^{-1}·K^{-2} and 0.068 mW·m^{-1}·K^{-2} are observed for S, while at 778 K, they show a plateau value of 0.38 mW·m^{-1}·K^{-2}

and 0.47 mW·m^{-1}·K^{-2} for Co$_2$ZrSn and Co$_2$HfSn samples, respectively. In most of the thermoelectric materials, the temperature dependence of the power factor shows a peak value in a narrow temperature range (approximately 100 K) [35], leading to a less efficient conversion when large temperature gradients are imposed. In the case of Co$_2$ZrSn and Co$_2$HfSn alloys, the extension of the power factor plateau across a wider temperature range (200–300 K) would allow obtaining optimal conversions also when temperature gradients of hundreds of degrees are used.
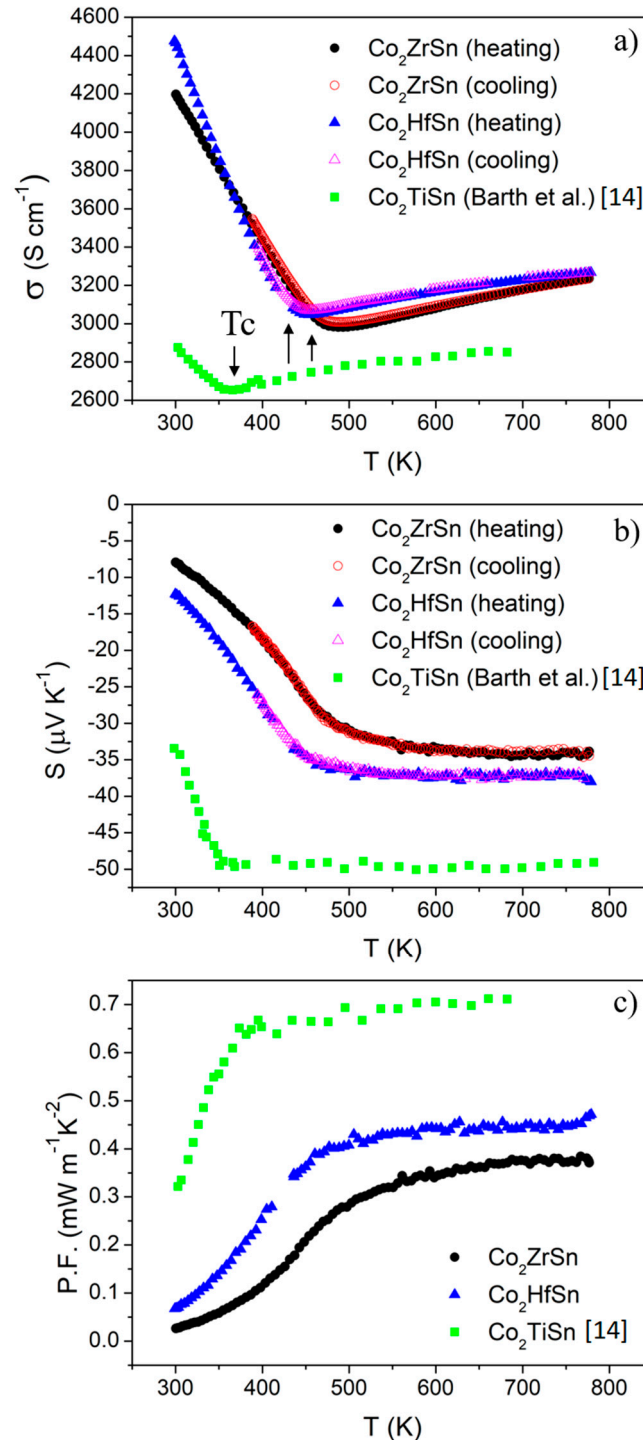
Figure 4. Electrical conductivity (**a**), Seebeck coefficient (**b**), and power factor (**c**) of the Co$_2$ZrSn and Co$_2$HfSn alloys. The transport properties of Co$_2$TiSn are shown as a comparison [14].

3.4. Effect of Composition on Electrical Conductivity, Seebeck Coefficient, and Power Factor

In the case of homogeneous solid solutions, the thermoelectric properties can be modulated on the basis of the fraction of the substituting elements. For example, the substitution effects are deeply known for the Fe_2VAl and Fe_2VAl-related FH compounds [36–39]. In fact, it is known that in multi-substituted Fe-based FH alloys, where the V atoms are replaced with isoelectronic elements (Nb and Ta), the thermoelectric performances result generally enhanced. The properties of the Fe_2XZ alloys can then be finely tuned by introducing specific quantities of substituents; therefore, they can be considered highly versatile compounds [37,38]. Thus, the implementation of these strategies on the Co-based FH alloys would be a considerable step forward in the application of this class of materials.

Potentially, isoelectronic substitution of X in Co_2XSn (X = Ti, Zr, Hf) might lead to a complete solubility over the whole compositional range, such as in (Zr,Hf)NiSn half-Heusler compound, or to partial solubility in a limited compositional range, such as in (Ti,Zr)NiSn and (Ti,Hf)NiSn half-Heusler alloys [40].

An overview of the transport properties measured at 673 K for the series of Co_2XSn alloys (X = Ti, Zr, Sn) is reported in Table 3 and they are shown as a function of the atomic number of X in Figure 5. Data for the Co_2TiSn compound have been taken from Ref. [14]. As far as the Seebeck coefficient is concerned, Co_2TiSn shows the highest absolute value of about 50 µV/K after T_C, while for Co_2HfSn and Co_2ZrSn compounds, values equal to 38 µV/K and 34 µV/K, respectively, can be observed. However, when the electrical conductivity is taken into account, Co_2TiSn is the compound with the lowest σ, while Co_2Hf and Co_2ZrSn display similar values of 3153 S/cm and 3214 S/cm, respectively. This leads to power factor values of 0.71 mW·m^{-1}·K^{-2}, 0.47 mW·m^{-1}·K^{-2} and 0.38 mW·m^{-1}·K^{-2} for Co_2TiSn, Co_2HfSn, and Co_2ZrSn compounds, respectively. All these values are quite high for metallic materials.

Table 3. Transport properties and Curie temperature of the Co_2XSn (X = Ti, Zr, Sn) series of full-Heusler alloys. All properties are reported at 673 K. T_C is the Curie temperature, S the Seebeck coefficient, σ the electrical conductivity, and PF is the power factor.

Alloy	T_C (K)	S (µV/K)	σ (S/cm)	PF (mW·m^{-1}·K^{-2})
Co_2TiSn [14]	360	−50	2851	0.71
Co_2ZrSn	465	−34	3157	0.38
Co_2HfSn	426	−38	3214	0.47

Considering Co_2TiSn and Co_2HfSn, which respectively show the largest Seebeck coefficient and electrical conductivity in the series, as end members, we could expect that if Ti is progressively substituted by Hf, the absolute value of the Seebeck coefficient would decrease, while the electrical conductivity would increase. As suggested by Figure 5d, the substitution of Ti with Hf would shift the Curie temperature at higher values, similarly to Co_2TiZ (Z = Si, Ge, Sn), where a fine tuning of T_C can be achieved by substituting the Z atom [14]. An increasing value of T_C can be useful in spintronics and spin-caloritronics applications, where it is desirable to have ferromagnetic materials even at high temperatures [10].
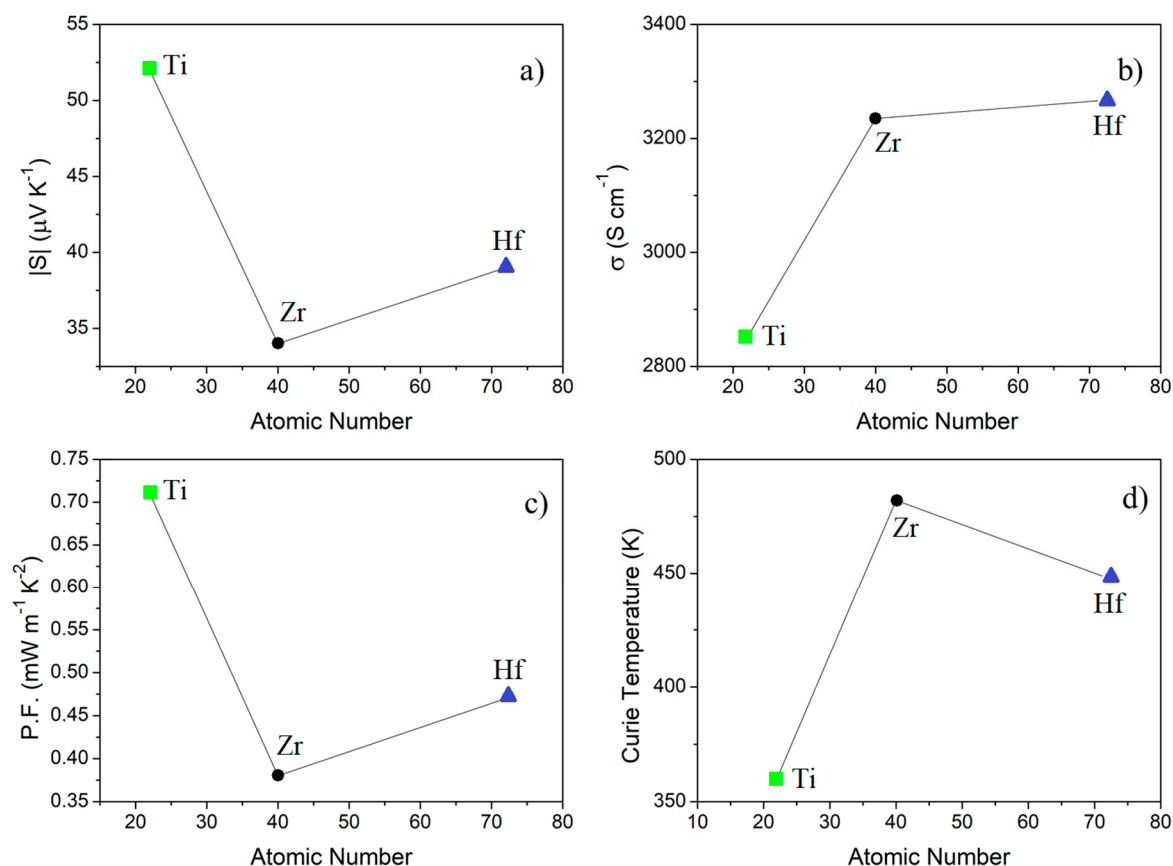
Figure 5. Trends of the transport properties (**a**): Seebeck coefficient; (**b**): electrical conductivity; (**c**): power factor) at 673 K, and Curie temperatures (**d**) of the Co_2XSn (X = Ti, Zr, Hf) series of full-Heusler alloys as a function of the atomic number of the X element.

4. Conclusions

In this work, the Co_2ZrSn and Co_2HfSn full-Heusler compounds were synthesized by arc melting and characterized from the structural and microstructural point of view. Vickers indentation allowed measuring the microhardness and deriving the fracture toughness, K_{IC}. Finally, the Seebeck coefficient and electrical conductivity were measured here for the first time. Both the alloys were obtained with sufficiently high purity as as-cast materials. The almost invariance of the relative abundances of phases after annealing reflects that the equilibrium is reached directly by solidification of the melt. The presence of small quantities of secondary phases, as previously reported by other studies [12], can be explained by the observed slight deviation of the samples from the nominal stoichiometry. The two alloys show high hardness (about 900 HV) and fracture toughness typical of ceramics (about 2 MPa·m$^{1/2}$). The transport properties of Co_2ZrSn and Co_2HfSn were measured for the first time. The Seebeck coefficient values are negative for both the alloys across the entire range of temperature explored (i.e., from room temperature up to 778 K), indicating an n-type behavior where electrons are the major charge carriers. For both the alloys, the absolute value of the Seebeck coefficient increases almost linearly between room temperature and the Curie temperature and shows a constant plateau after T_C instead of the typical peak shape. No sign of hysteresis was shown after thermal cycling, indicating the good thermal stability of the alloys in the considered temperature range. Concerning the electrical conductivities, both the compounds are found to behave similar to metals before T_C, and similar to semiconductors after T_C; furthermore, the values of σ set in almost constant plateaus at temperatures sufficiently higher than the Curie point. The power factor of the alloys also exhibits a quite linear increase, followed by a constant ceiling, reflecting the trends of the Seebeck coefficients that are the dominant contributors to the power factor. Taking into account the information available in the

literature for the Co$_2$TiSn compound, we ordered the transport properties of the Co$_2$XSn (X = Ti, Zr, Hf) family of full-Heusler compounds. While Co$_2$ZrSn and Co$_2$HfSn show larger electrical conductivities, Co$_2$TiSn shows a larger absolute value of the Seebeck coefficient. Thus, Co$_2$TiSn shows the largest power factor in the series. The possible effects of the substitution of Ti with Hf on the electronic transport properties were discussed on the basis of the observed experimental trends.

References

1. Poon, S.J. Recent advances in thermoelectric performance of half-heusler compounds. *Metals* **2018**, *8*, 989. [CrossRef]

2. Sakurada, S.; Shutoh, N. Effect of Ti substitution on the thermoelectric properties of (Zr, Hf) NiSn half-Heusler compounds. *Appl. Phys. Lett.* **2005**, *86*, 82105. [CrossRef]

3. Fu, C.; Bai, S.; Liu, Y.; Tang, Y.; Chen, L.; Zhao, X.; Zhu, T. Realizing high figure of merit in heavy-band p-type half-Heusler thermoelectric materials. *Nat. Commun.* **2015**, *6*, 1–7. [CrossRef]

4. Gürth, M.; Rogl, G.; Romaka, V.V.; Grytsiv, A.; Bauer, E.; Rogl, P. Thermoelectric high ZT half-Heusler alloys Ti1- x- yZrxHfyNiSn (0 ≤ x ≤ 1; 0 ≤ y ≤ 1). *Acta Mater.* **2016**, *104*, 210–222. [CrossRef]

5. Rogl, G.; Yubuta, K.; Romaka, V.V.; Michor, H.; Schafler, E.; Grytsiv, A.; Bauer, E.; Rogl, P. High-ZT half-Heusler thermoelectrics, Ti0. 5Zr0. 5NiSn and Ti0.5Zr0.5NiSn0.98Sb0.02: Physical properties at low temperatures. *Acta Mater.* **2019**, *166*, 466–483. [CrossRef]

6. Hirohata, A.; Kikuchi, M.; Tezuka, N.; Inomata, K.; Claydon, J.S.; Xu, Y.B.; van der Laan, G. Heusler alloy/semiconductor hybrid structures. *Curr. Opin. Solid State Mater. Sci.* **2006**, *10*, 93–107. [CrossRef]

7. Felser, C.; Fecher, G.H. *Spintronics: From Materials to Devices*; Springer Science & Business Media: Dordrecht, The Netherlands, 2013.

8. Graf, T.; Felser, C.; Parkin, S.S.P. Simple rules for the understanding of Heusler compounds. *Prog. Solid State Chem.* **2011**, *39*, 1–50. [CrossRef]

9. Lee, S.C.; Lee, T.D.; Blaha, P.; Schwarz, K. Magnetic and half-metallic properties of the full-Heusler alloys Co 2TiX (X = Al, Ga; Si, Ge, Sn; Sb). *J. Appl. Phys.* **2005**, *97*, 14–17. [CrossRef]

10. Boona, S.R.; Myers, R.C.; Heremans, J.P. Spin caloritronics. *Energy Environ. Sci.* **2014**, *7*, 885–910. [CrossRef]

11. Beretta, D.; Neophytou, N.; Hodges, J.M.; Kanatzidis, M.G.; Narducci, D.; Martin-Gonzalez, M.; Beekman, M.; Balke, B.; Cerretti, G.; Tremel, W.; et al. Thermoelectrics: From history, a window to the future. *Mater. Sci. Eng. R Rep.* **2019**, *138*, 100501. [CrossRef]

12. Ziebeck, K.R.A.; Webster, P.J. A neutron diffraction and magnetization study of Heusler alloys containing Co and Zr, Hf, V or Nb. *J. Phys. Chem. Solids* **1974**, *35*, 1–7. [CrossRef]

13. De Souza, S.D.; Saxena, R.N.; Shreiner, W.; Zawislak, F.C. Magnetic hyperfine fields in Heusler alloys Co YZ (Y = Ti, Zr; Z = Al, Ga, Sn). *Hyperfine Interact.* **1987**, *34*, 431–434. [CrossRef]

14. Barth, J.; Fecher, G.H.; Balke, B.; Graf, T.; Shkabko, A.; Weidenkaff, A.; Klaer, P.; Kallmayer, M.; Elmers, H.J.; Yoshikawa, H.; et al. Anomalous transport properties of the half-metallic ferromagnets Co$_2$TiSi, Co$_2$TiGe and Co$_2$TiSn. *Philos. Trans. R. Soc. A Math. Phys. Eng. Sci.* **2011**, *369*, 3588–3601. [CrossRef] [PubMed]

15. Babiker, A.S.; Gao, G.; Yao, K. Half-metallicity and magnetism of Heusler alloys Co$_2$HfZ (Z = Al, Ga, Ge, Sn). *J. Magn. Magn. Mater.* **2017**, *441*, 356–360. [CrossRef]

16. Bekenov, L.V.; Antonov, V.N.; Shpak, A.P.; Yaresko, A.N. Electronic structure and excited-state properties of Co$_2$TiSn and Co$_2$ZrSn from ab initio calculations. *Condens. Matter Phys.* **2005**, *8*, 565–577. [CrossRef]

17. Curtarolo, S.; Setyawan, W.; Hart, G.L.W.; Jahnatek, M.; Chepulskii, R.V.; Taylor, R.H.; Wang, S.; Xue, J.; Yang, K.; Levy, O.; et al. AFLOW: An automatic framework for high-throughput materials discovery. *Comput. Mater. Sci.* **2012**, *58*, 218–226. [CrossRef]

18. Lutterotti, L.; Matthies, S.; Wenk, H.-R. MAUD (material analysis using diffraction): A user friendly Java program for Rietveld texture analysis and more. In Proceedings of the Twelfth International Conference on Textures of Materials (ICOTOM-12), Montréal, QC, Canada, 9–13 August 1999; Volume 1, p. 1599.

19. Boldrini, S.; Famengo, A.; Montagner, F.; Battiston, S.; Fiameni, S.; Fabrizio, M.; Barison, S. Test rig for high-temperature thermopower and electrical conductivity measurements. *J. Electron. Mater.* **2013**, *42*, 1319–1323. [CrossRef]

20. *International Centre for Diffraction Data, Powder Diffraction File*; ICDD: Newton Square, PA, USA, 1997.

21. Villars, P.; Prince, A.; Okamoto, H. *Handbook of Ternary Alloy Phase Diagrams*; ASM International, Materials Park: Novelty, OH, USA, 1995; Volume 5.

22. Ponton, C.B.; Rawlings, R.D. Vickers indentation fracture toughness test Part 1 Review of literature and formulation of standardised indentation toughness equations. *Mater. Sci. Technol.* **1989**, *5*, 865–872. [CrossRef]

23. Roebuck, B.; Bennett, E.G.; Lay, L.A.; Morrell, R. *The Measurement of Palmqvist Toughness for Hard and Brittle Materials*; National Physical Laboratory: Teddington, UK, 2008.

24. Madeiros, E.E.; Dias, A.M.S. Experimental and numerical analysis of Vickers hardness testing. *Int. J. Res. Rev. Appl. Sci.* **2013**, *17*, 9–18.

25. Faisal, N.H.; Ahmed, R.; Prathuru, A.K.; Spence, S.; Hossain, M.; Steel, J.A. An improved Vickers indentation fracture toughness model to assess the quality of thermally sprayed coatings. *Eng. Fract. Mech.* **2014**, *128*, 189–204. [CrossRef]

26. Sktani, Z.D.I.; Rejab, N.A.; Ratnam, M.M.; Ahmad, Z.A. Fabrication of tougher ZTA ceramics with sustainable high hardness through (RSM) optimisation. *Int. J. Refract. Met. Hard Mater.* **2018**, *74*, 78–86. [CrossRef]

27. Liang, K.M.; Orange, G.; Fantozzi, G. Evaluation by indentation of fracture toughness of ceramic materials. *J. Mater. Sci.* **1990**, *25*, 207–214. [CrossRef]

28. Bradt, R.C. *Fracture Mechanics on Ceramics: 3rd International Symposium Held July 15–17, 1983, at the Pennsylvania State University in University Park, Pennsylvania*; Plenum Press: New York, NY, USA, 1983.

29. Shetty, D.K.; Wright, I.G.; Mincer, P.N.; Clauer, A.H. Indentation fracture of WC-Co cermets. *J. Mater. Sci.* **1985**, *20*, 1873–1882. [CrossRef]

30. Ashby, M.F. *Materials Selection in Mechanical Design*, 4th ed.; Elsevier: Kidlington, UK, 2011.

31. Rogl, G.; Grytsiv, A.; Gürth, M.; Tavassoli, A.; Ebner, C.; Wünschek, A.; Puchegger, S.; Soprunyuk, V.; Schranz, W.; Bauer, E.; et al. Mechanical properties of half-Heusler alloys. *Acta Mater.* **2016**, *107*, 178–195. [CrossRef]

32. Ikeda, K. Electrical resistivity of Laves phase compounds containing transition elements II. Co$_2$A (A = Ti, Y, Zr, and Nb). *J. Phys. Soc. Jap.* **1977**, *42*, 1541–1546. [CrossRef]

33. Li, S.X.; Yu, K.M.; Wu, J.; Jones, R.E.; Walukiewicz, W.; Ager, J.W.; Shan, W.; Haller, E.E.; Lu, H.; Schaff, W.J. Fermi-level stabilization energy in group III nitrides. *Phys. Rev. B Condens. Matter Mater. Phys.* **2005**, *71*, 1–4. [CrossRef]

34. Dashevsky, Z.; Shusterman, S.; Dariel, M.P.; Drabkin, I. Thermoelectric efficiency in graded indium-doped PbTe crystals. *J. Appl. Phys.* **2002**, *92*, 1425–1430. [CrossRef]

35. Mehdizadeh Dehkordi, A.; Zebarjadi, M.; He, J.; Tritt, T.M. Thermoelectric power factor: Enhancement mechanisms and strategies for higher performance thermoelectric materials. *Mater. Sci. Eng. R Reports* **2015**, *97*, 1–22. [CrossRef]

36. Alleno, E. Review of the thermoelectric properties in nanostructured Fe2VAl. *Metals* **2018**, *8*, 864. [CrossRef]

37. Kurosaki, K.; Muta, H.; Endo, Y.; Charoenphakdee, A.; Uno, M.; Yamanaka, S. Effect of Nb substitution for V on the thermoelectric properties of Fe2VAl. *J. Alloys Compd.* **2009**, *486*, 507–510. [CrossRef]

38. Al-Yamani, H.; Hamad, B. Thermoelectric Properties of Fe2VAl and Fe2V0.75M0.25Al (M = Mo, Nb, Ta) Alloys: First-Principles Calculations. *J. Electron. Mater.* **2016**, *45*, 1101–1114. [CrossRef]

39. Hinterleitner, B.; Knapp, I.; Poneder, M.; Shi, Y.; Müller, H.; Eguchi, G.; Eisenmenger-Sittner, C.; Stöger-Pollach, M.; Kakefuda, Y.; Kawamoto, N.; et al. Thermoelectric performance of a metastable thin-film Heusler alloy. *Nature* **2019**, *576*, 85–90. [CrossRef]

40. Kimura, Y.; Chai, Y.W. Ordered Structures and Thermoelectric Properties of MNiSn (M = Ti, Zr, Hf)-Based Half-Heusler Compounds Affected by Close Relationship with Heusler Compounds. *JOM* **2015**, *67*, 233–245. [CrossRef]